ELSEVIER

Contents lists available at ScienceDirect

# Journal of Electroanalytical Chemistry

journal homepage: www.elsevier.com/locate/jelechem





# Promotion of nitrate reduction reaction activity by $Co_3O_4@MoS_2$ Particle-Support system

Yanli Zhang, Jiuqing Xiong, Shihai Yan<sup>\*</sup>, Bingping Liu<sup>\*</sup>

College of Chemistry and Pharmaceutical Sciences, Qingdao Agricultural University, Qingdao, 266109, China

#### ARTICLE INFO

 $\label{eq:keywords:} \textit{Keywords:} \\ \text{Electrochemical nitrate reduction reaction} \\ \text{Co}_3\text{O}_4\text{@MoS}_2 \\ \text{Particle-support system} \\ \text{Synergistic effect} \\ \text{Density functional theory} \\$ 

#### ABSTRACT

Electrochemical reduction of nitrate to  $NH_3$  is a very promising alternative reaction to the Haber-Bosch process, and it is necessary to develop the efficient electrocatalysts. In this study, a particle-support mode  $Co_3O_4$  catalyst was synthesized with ZIF-67 as the precursor, and then dispersed on  $MoS_2$  nanoflowers by hydrothermal method. The  $Co_3O_4$  is anchored to  $MoS_2$  by forming Co-S coordination bond. Furthermore, the particle-supported  $Co_3O_4$  exhibits better performance than  $Co_3O_4$  alone, as is manifested by higher Faradaic efficiencies and  $NH_3$  yield rate at - 0.64 V (52.69% vs 32.03%; 4539.61  $\mu$ g h<sup>-1</sup>  $mg_{cat}^{-1}$  vs 2048.63  $\mu$ g h<sup>-1</sup>  $mg_{cat}^{-1}$ ), lower energy barriers (0.96 eV vs 1.19 eV), and better electronic conductivity (Bandwidth: 0.581 eV vs 0.613 eV). In addition, this research provides an effective solution to solve the aggregation problem of metal oxide nanoparticles.

#### 1. Introduction

Ammonia is the basis of modern agriculture, heavy industry, pharmaceutical industry, and fertilizer production [1,2]. In addition, it has made outstanding contributions to the growth and development of animals and plants, and is considered as a renewable carbon-free hydrogen-rich energy carrier with high hydrogen content of 17.7 wt% [3–6]. With the development of society, the demand for ammonia has increased sharply. A large proportion of NH<sub>3</sub> is fabricated via the traditional Haber-Bosch process with the nitrogen and hydrogen as the raw materials under the harsh conditions with high temperature (400 – 500 °C) and pressure (150 – 300 atm) [7–9], and the process consumes about 1–3% of annual global energy and generates huge CO<sub>2</sub> emission [10]. Beyond that, it has a poor energy efficiency with the low conversion constrained by thermodynamics and requiring large centralized infrastructure [11].

More recently, electrochemical nitrogen reduction reaction (eNRR) has been paid extensive attention [12] due to its simplicity, safety, and environmental friendship in contrast with other alternative methods, such as photocatalysis [13] and enzymatic catalysis [14]. In eNRR, nitrogen reacts with water to generate ammonia by a certain voltage under mild conditions [15]. However, the high dissociation energy of N=N (941 kJ mol<sup>-1</sup>) and the competitive reaction of hydrogen evolution reaction (HER) lead to lower generation rate of ammonia and lower faraday efficiency (FE%), which is not suitable for industrial production

[4,12,16]. Compared with eNRR, electrochemical nitrate reduction reaction (eNO $_3$ RR) avoids the above shortcomings effectively and attracted extensive attention. In nitrate ions (NO $_3$ ), dissociation energy of N-O bond is 204 kJ mol $^{-1}$  only and NO $_3$  is very soluble in water, both of which strongly promote the reduction from NO $_3$  to NH $_3$  and the rate is distinctly larger than that of NRR reaction [17,18]. In addition, the raw material of NO $_3$  exists widely in the environment as a pollutant, produced by chemical and agricultural industries [19,20]. Therefore, the conversion of NO $_3$  into NH $_3$  can not only solve environmental pollutants, but also obtain ammonia resources, which is of great research value.

So far, several groups have reported cobalt-based oxides as cathode catalysts for eNO<sub>3</sub>RR because of Co<sub>3</sub>O<sub>4</sub> is one of the spinel oxides with flexible ionic arrangement and multivalent structure [3,17,21,22,39-41]. The results demonstrate that  $Co_3O_4$  is indeed active for eNO<sub>3</sub>RR, but with a low ammonia yield (283  $\mu$ g mg<sup>-1</sup>h<sup>-1</sup>) [23,24]. Co<sub>3</sub>O<sub>4</sub> nanoparticles are prone to aggregation due to its high surface energy [25], the most common solution is to disperse the nanoparticles on a template. For example, Zhou et al. used the template method to disperse Co<sub>3</sub>O<sub>4</sub> nanoparticles onto TiO<sub>2</sub> nanosheets. It was pointed out that the supports could affect or even dominate the catalytic activity and selectivity of the nanoparticles because atomic geometry and electronic structure of the active site at the interface of nanoparticles and support could be regulated [26]. Therefore, a support-like composite might effectively solve the aggregation problem of Co<sub>3</sub>O<sub>4</sub> nanoparticles by

E-mail addresses: shyan@qau.edu.cn (S. Yan), bpliu@qau.edu.cn (B. Liu).

<sup>\*</sup> Corresponding authors.

increasing the specific surface area to add more active sites, while the electron transfer between the carrier and nanoparticles enhances the electrical conductivity of  $\text{Co}_3\text{O}_4$ , thus improves the activity of the reaction center. Molybdenum disulfide (MoS<sub>2</sub>) has been widely reported in NRR for its high chemical stability and large specific surface area, where the base of 2H-MoS<sub>2</sub> has a large numbers of sulfur atoms that can bond with transition metals to form coordination bonds covering the surface [27,28,42], and its flower morphology provides a good platform for later loading. The structure of MoS<sub>2</sub> nanoflower has a larger loading area than TiO<sub>2</sub> nanosheet. The  $\text{Co}_3\text{O}_4$  anchored on MoS<sub>2</sub> nanoflowers ( $\text{Co}_3\text{O}_4$ @MoS<sub>2</sub>) is expected to be synergistic effect of  $\text{Co}_3\text{O}_4$  and MoS<sub>2</sub> to improve the efficiency of eNO<sub>3</sub>RR.

The support of  $MoS_2$  nanoflowers in  $Co_3O_4@MoS_2$  composite can promote the electron transfer and prevent the aggregation of  $Co_3O_4$  nanoparticles. The  $Co_3O_4$  nanoparticles are synthesized by pyrolysis of zeolitic imidazolate frameworks (ZIFs) precursor to reduce the size. The  $Co_3O_4@MoS_2$  catalyst exhibits outstanding catalytic performance for eNO<sub>3</sub>RR with the NH<sub>3</sub> yield rate of 4539.61  $\mu g \ h^{-1} \ mg_{cat}^{-1}$  and the Faradaic efficiency (FE) of 52.69% at - 0.64 V. To explore the reaction mechanism and the catalytic principle, the density functional theory (DFT) calculations are performed for NO $_3^-$  reduction to NH $_3^-$  on the active site of the catalysts. It is elucidated that the improved performance comes from the synergistic effect of  $Co_3O_4$  and  $MoS_2$ , as well as better electronic conductivity of  $Co_3O_4@MoS_2$  with lower energy barriers (0.96 eV).

#### 2. Experimental section and computational method

#### 2.1. Materials

Cobalt chloride hexahydrate (CoCl2·6H2O), isopropanol, sodium hydroxide (NaOH), sodium nitroferricyanide(C5FeN6Na2O·2H2O), potassium nitrate (KNO<sub>3</sub>), sulfonamide were purchased from Sinopharm Chemical Reagent Co., Ltd (China). Methanol, thiourea (CH<sub>4</sub>N<sub>2</sub>S), sodium citrate (C<sub>6</sub>H<sub>5</sub>Na<sub>3</sub>O<sub>7</sub>), sodium hypochlorite (NaClO), anhydrous sodium sulfate (Na<sub>2</sub>SO<sub>4</sub>) were purchased from Tianjin Fuyu Fine Chemical Co., Ltd., Tianjin BASF Chemical Co., Ltd., Tianjin Bodi Chemical Co., Ltd., Tianjin Yongda Chemical Reagent Co., Ltd., and Tianjin Dingshengxin Chemical Co., Ltd. respectively. Hexaammonium heptamolybdate tetrahydrate ((NH<sub>4</sub>)<sub>6</sub>Mo<sub>7</sub>O<sub>24</sub>·4H<sub>2</sub>O), 2-Methylimidazole(C<sub>4</sub>H<sub>6</sub>N<sub>2</sub>), Nafion (5 wt%) were purchased from Shanghai Silver Iodine Chemical Co., Ltd., Shanghai McLean Biochemical Technology Co., Ltd., and Aladdin Ltd.(China) respectively. Salicylic acid (C<sub>7</sub>H<sub>6</sub>O<sub>3</sub>) and ethanol were purchased from Laiyang Kangde Chemical Co., Ltd.(China). Phosphoric acid (H<sub>3</sub>PO<sub>4</sub>) was bought from Beijing Chemical Industry Co., Ltd (China). N-(1-naphthyl) ethylenediamine dihydrochloride was purchased from Tianjin Aopuseng Chemical Co., Ltd.

#### 2.2. Catalyst synthesis

#### 2.2.1. Synthesis of Co<sub>3</sub>O<sub>4</sub> nanoparticles

CoCl $_2$ -GH $_2$ O and 2-Methylimidazole were dissolved in the binary mixture of 40 mL methanol and 40 mL water, then ultrasonic oscillated for 10 mins. The mixture was allowed to stand overnight at room temperature for precipitation reaction and the purple precipitate was collected by centrifugation followed by washing several times with methanol. Finally, the dried sample was obtained under vacuum as the precursor of  $\rm Co_3O_4$  Nanoparticles and named as ZIF-67 (a metal–organic framework material). The ZIF-67 precursor was placed in the furnace and heated to 500 °C for 10 h with the heating rate of 2 °C/min to prepare  $\rm Co_3O_4$  nanoparticles [43].

## 2.2.2. Synthesis of MoS2 nanoflowers

 $(NH_4)_6Mo_7O_{24}\cdot 4H_2O$  and  $CH_4N_2S$  were dissolved in 40 mL ultrapure water, and stired for 1 h. The resulting solution moved into a Teflon-

equipped stainless-steel autoclave and heated at 220 °C for 18 h. The product was collected by centrifugation and washed several times with ethanol. Then, the  $MoS_2$  catalyst were obtained by drying overnight in a vacuum oven at 60 °C [44,45].

#### 2.2.3. Synthesis of Co<sub>3</sub>O<sub>4</sub>@MoS<sub>2</sub>

A solution of the same steps as the above 2.2.2 to make  $MoS_2$  nanoflowers, mixed with  $Co_3O_4$  nanoparticles (100 mg /150 mg /200 mg), and then stirred for 0.5 h. The mixed solution was moved into a Teflon-equipped stainless-steel autoclave for heating, washing, and drying under the same conditions as the step of 2.2.2. Then got the  $Co_3O_4@MoS_2$  catalyst.

#### 2.3. Characterization of samples

The morphology and microstructure of all prepared samples were analyzed by scanning electron microscopy (SEM, ZEISS Gemini SEM 300). The crystal structure of the catalyst was characterized by X-ray diffraction (XRD, Rigaku Smart Lab SE). The composition and state of the catalyst surface were determined by X-ray photoelectron spectroscopy (XPS, Thermo Scientific K-Alpha). The concentration of NH<sub>3</sub> was measured using a UV-3900 spectrophotometer.

#### 2.4. Preparation of the working electrode

3 mg of catalyst and  $20~\mu L$  of Nafion solution were dispersed into  $500~\mu L$  of isopropanol and were ultrasonicated for 1~h to form a uniform ink. Then  $40~\mu L$  of ink was evenly dropped on the glassy carbon electrode with a loading of  $0.23~mg~cm^{-2}$  to prepare the working electrode and the thickness is almost unmeasurable due to the thin layer on the GC surface.

#### 2.5. Electrochemical measurements

Electrochemical measurements were performed in an H-type electrolytic cell with a standard three-electrode system separated by a nafion 117 membrane. In this system, the catalyst was supported on a glassy carbon electrode as the working electrode, a graphite rod and a saturated Ag/AgCl electrode as the counter and reference electrodes, respectively. All potentials in this paper were measured by saturated Ag/AgCl and converted to the reversible hydrogen electrode potential by E (vs. RHE) = E (vs. Ag/AgCl) + 0.61 as the reference scalar. The performance test of eNO<sub>3</sub>RR was carried out in the electrolyte (30 mL) of 0.1 M Na<sub>2</sub>SO<sub>4</sub> and 0.2 M KNO<sub>3</sub>. Before the test, Ar gas was introduced into the cathodic electrolytic cell for 15 min to remove the residual air in the system, and then Ar was continued to be introduced and reacted at an external potential for 1 h. After the test is completed, the electrolyte is collected and disposed of as waste liquid to avoid contamination.

#### 2.6. Determination of NH<sub>3</sub>

The concentration of NH $_3$  was determined by UV–Vis spectrophotometer using a modified indophenol blue method. Take 2 mL of the reacted catholyte and add 1 mL of 0.05 M NaClO, 2 mL of a mixture of 1 M NaOH containing 5 wt% salicylic acid and 5 wt% sodium citrate, and 0.2 mL of 1 wt%  $\rm C_5FeN_6Na_2O$  (sodium nitroferricyanide). Then, the absorbance at 665 nm was measured by UV–Vis spectrophotometer after standing at room temperature for 2 h. And concentration-absorbance curves were drawn using a series of standard ammonium chloride solutions.

#### 2.7. Determination of NO2

Firstly, 0.1~g of N-(1-naphthyl) ethylenediamine dihydrochloride, 1~g of sulfonamide and 2.94~mL of  $H_3PO_4$  in 50~mL  $H_2O$  and mixed thoroughly as the color reagent. Take 1~mL of the reacted catholyte and add 1~mL color reagent, 2~mL  $H_2O$  to stand for 10~min, and the absorption

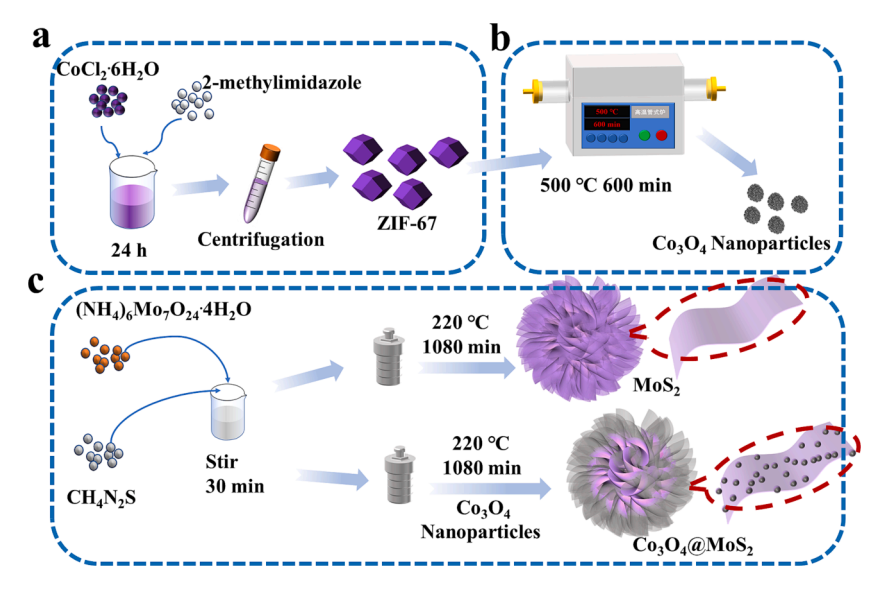


Fig. 1. Schematic diagrams to illustrate the synthesis of (a) ZIF-67, (b) Co<sub>3</sub>O<sub>4</sub> nanoparticles, (c) MoS<sub>2</sub> and Co<sub>3</sub>O<sub>4</sub>@MoS<sub>2</sub>.

intensity at a wavelength of 540 nm is recorded by UV–Vis absorption spectra.

# 2.8. Calculation of the $NH_3$ yield and faradic efficiency (FE)

The FE calculation formula for electrocatalytic  $NO_3^-NH_3$  conversion is calculated as follows:

$$FE_{NH_3} = \frac{8 \times F \times C_{NH_3} \times V}{17 \times Q}$$

where F is the Faraday constant,  $C_{NH_3}$  is the measured NH<sub>3</sub> concentration, V is the volume of catholyte, and Q is the total charge.

The formula for calculating the yield of NH<sub>3</sub> is as follows:

$$Yield_{NH_3} = \frac{C_{NH_3} \times V}{t \times m_{cat}}$$

where t is the time of the electrocatalytic reaction and m is the catalyst loading.

## 2.9. Computational details

Density functional theory (DFT) calculations were performed using the first-principle computational simulation package (VASP 5.4.4) developed by Hafner's group [29,30]. The generalized gradient

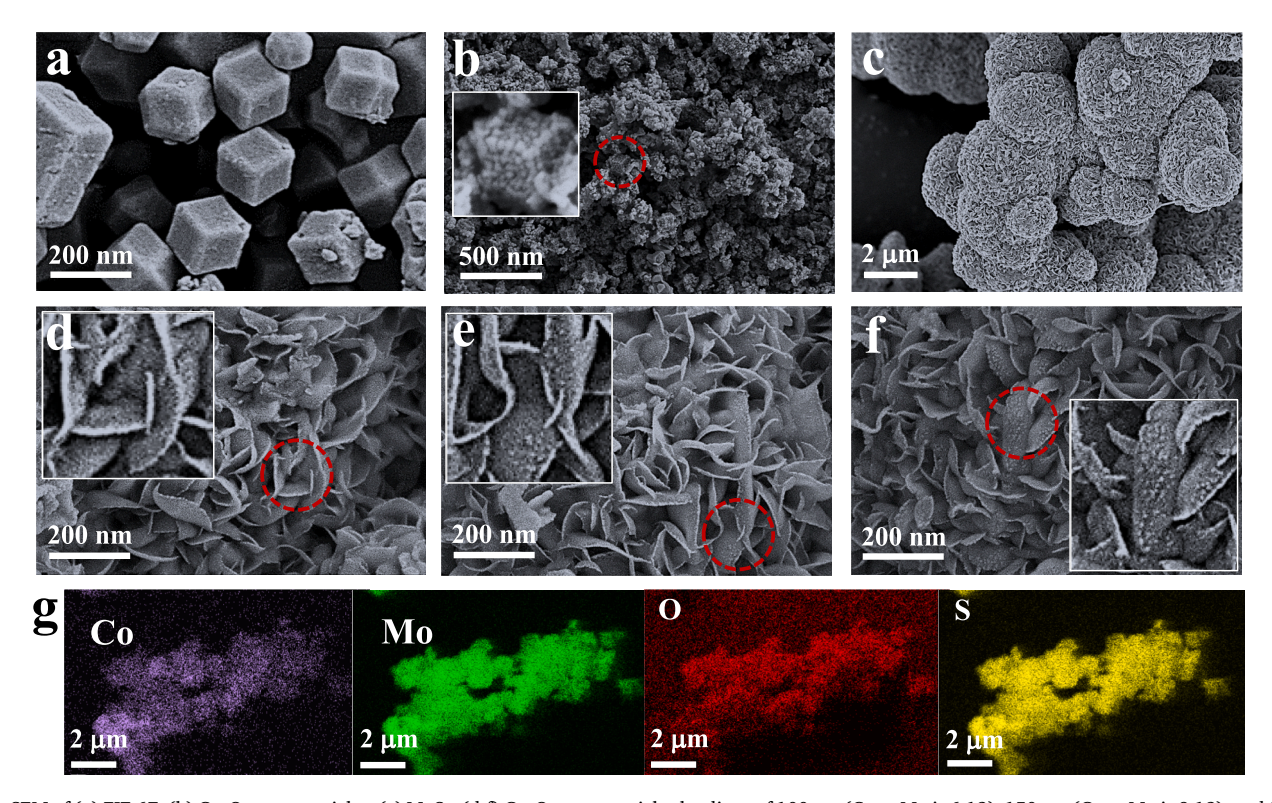


Fig. 2. SEM of (a) ZIF-67, (b)  $Co_3O_4$  nanoparticles, (c)  $MoS_2$ , (d-f)  $Co_3O_4$  nanoparticles loadings of 100 mg (Co to Mo is 6:13), 150 mg (Co to Mo is 9:13), and 200 mg (Co to Mo is 12:13) in  $Co_3O_4$ @ $MoS_2$ , respectively. (g) EDX mapping images of  $Co_3O_4$ @ $MoS_2$  with the ratio of Co to Mo is 9:13.

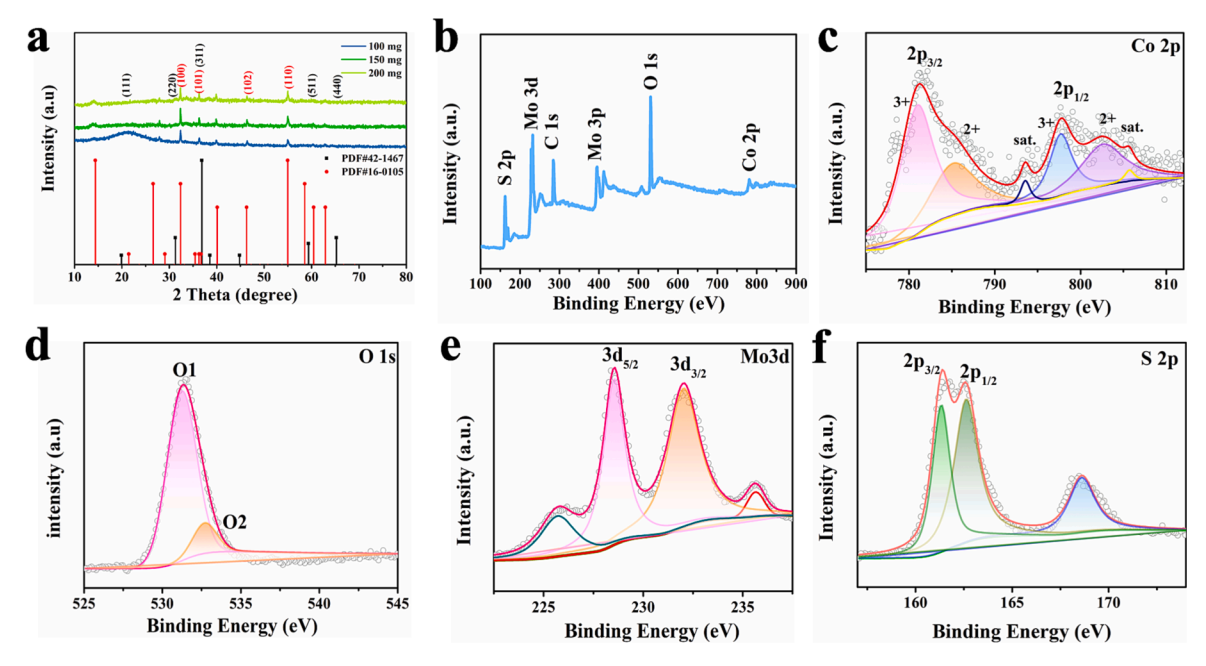


Fig. 3. XRD patterns of (a)  $Co_3O_4$  nanoparticles loadings of 100 mg (Co to Mo is 6:13), 150 mg (Co to Mo is 9:13), and 200 mg (Co to Mo is 12:13) in  $Co_3O_4$ @MoS<sub>2</sub>. The XPS of  $Co_3O_4$ @MoS<sub>2</sub> (Co to Mo is 9:13) measured spectra are (b) full spectrum, (c)  $Co_3O_4$  (d)  $Co_3O_4$  (e) Mo 3d, (f)  $Co_3O_4$  (f)  $Co_3O_4$ 

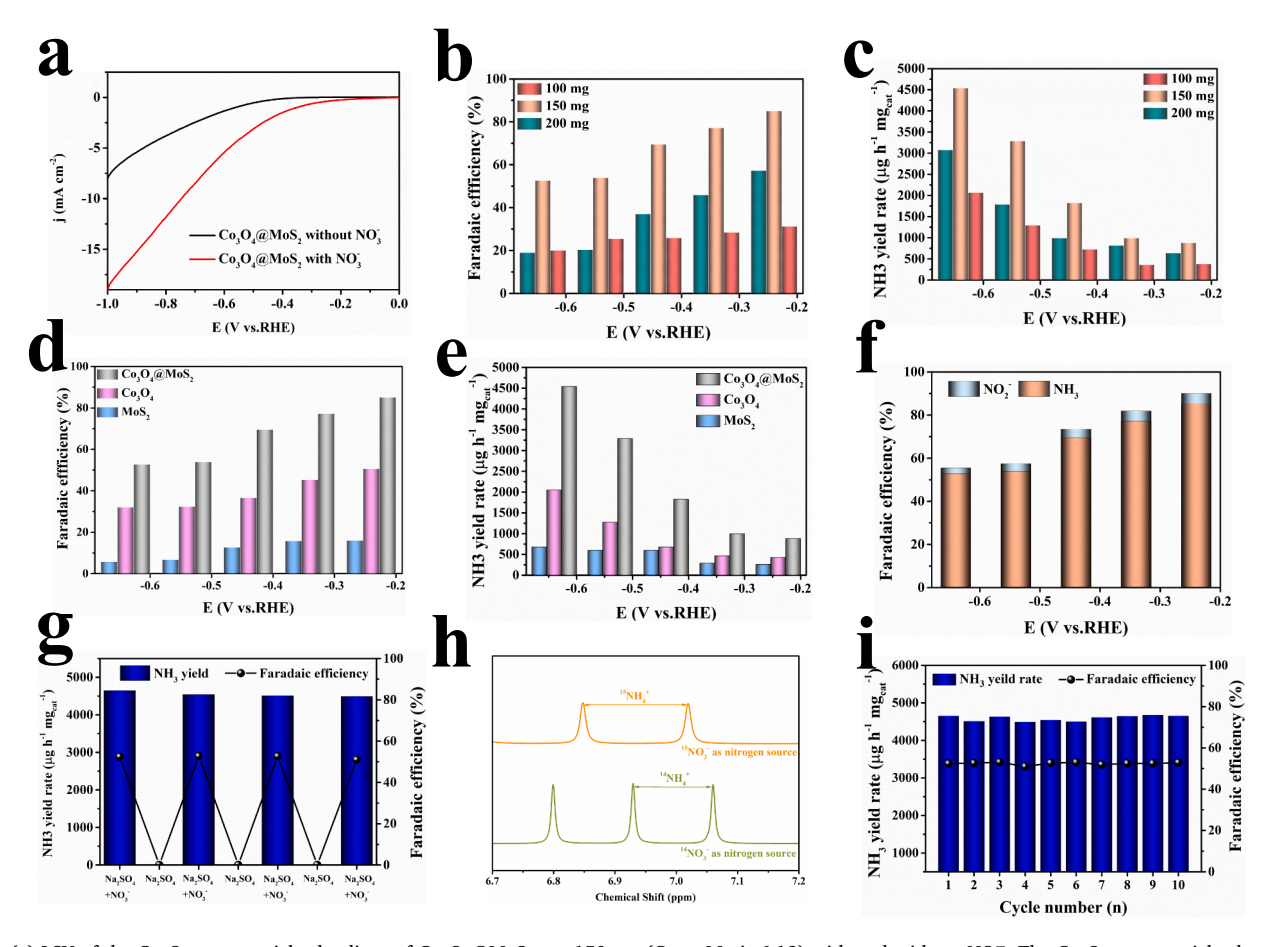


Fig. 4. (a) LSV of the  $Co_3O_4$  nanoparticles loadings of  $Co_3O_4$ @MoS<sub>2</sub> are 150 mg (Co to Mo is 6:13) with and without  $NO_3^-$ . The  $Co_3O_4$  nanoparticles loadings of  $Co_3O_4$ @MoS<sub>2</sub> are 100 mg (Co to Mo is 6:13), 150 mg (Co to Mo is 9:13), 200 mg (Co to Mo is 12:13) of (b) NH<sub>3</sub> Faradaic efficiency and (c) NH<sub>3</sub> yield rate, respectively. The (d) Faradaic efficiency and (e) NH<sub>3</sub> yield rate of MoS<sub>2</sub>,  $Co_3O_4$ ,  $Co_3O_4$ @MoS<sub>2</sub> (Co to Mo is 9:13). (f) The distribution of products  $NO_2^-$  and NH<sub>3</sub> between - 0.24 and - 0.64 V for  $Co_3O_4$ @MoS<sub>2</sub> (Co to Mo is 9:13). (g) NH<sub>3</sub> yield rate and Faradaic efficiency in alternating cycles between with and without  $NO_3^-$  electrolyte of  $Co_3O_4$ @MoS<sub>2</sub>(Co to Mo is 9:13) at - 0.64 V. (h)  $^1$ H nuclear magnetic resonance (NMR) spectrum of the electrolyte after eNO<sub>3</sub>RR on  $Co_3O_4$ @MoS<sub>2</sub>(Co to Mo is 9:13) at - 0.64 V with  $^{15}NO_3^-$  and  $^{14}NO_3^-$  as nitrogen sources. (i) 10-cycle test of  $Co_3O_4$ @MoS<sub>2</sub>(Co to Mo is 9:13) at - 0.64 V.

approximation of the Perdew-Burke-Enzzerhof (GGA-PBE) exchange–correlation functional and the pseudo-potential determination by Projector-Augmented-Wave (PAW) were used to optimize the structure and calculate the electronic energy [31,32]. A ( $3\times3\times1$ ) Monkhorst–Pack k-point grid was employed to sample at the Brillouin zone gamma points. At the same time, the cutoff energy was set to 500 eV and the self-consistent calculation was performed with a total energy of  $10^{-5}$  eV and a force of -0.05 eV/Å per atom. The DFT-D2 method was also employed to approximate the van der Waals interaction and the adsorption energy of each intermediate on the catalyst [33]. The Gibbs free energy is determined by using a standard vibrational correction for entropy, calculated as  $\Delta G = \Delta E + \Delta ZPE - T\Delta S$ , where  $\Delta E$  is the electron energy difference,  $\Delta ZPE$  is the zero-point correction energy, T is the reaction temperature (298.15 K), and  $\Delta S$  is the entropy change.

#### 3. Results and discussion

#### 3.1. Synthesis and characterizations of electrocatalysts

The composite of  $\text{Co}_3\text{O}_4@\text{MoS}_2$  was prepared following the scheme shown in Fig. 1. Firstly, the metal–organic frameworks precursor of ZIF-67 was obtained by precipitation reaction shown in Fig. 1a. Then, ZIF-67 was calcined at 500 °C for 10 h to obtain  $\text{Co}_3\text{O}_4$  nanoparticles (Fig. 1b), which was dispersed into the reactants to prepare the  $\text{Co}_3\text{O}_4@\text{MoS}_2$  composite by hydrothermal method shown in Fig. 1c. The morphologies of all the samples were characterized by scanning electron microscopy (SEM) (Fig. 2), including ZIF-67,  $\text{Co}_3\text{O}_4$  nanoparticles,  $\text{MoS}_2$ , and  $\text{Co}_3\text{O}_4@\text{MoS}_2$ .

ZIF-67 exhibits a rhombic dodecahedron morphology with a uniform particle size of 100 nm (Fig. 2a). After calcination,  $\text{Co}_3\text{O}_4$  nanoparticles maintained the original dodecahedron framework with a diameter of 40 nm (Fig. 2b). When  $\text{MoS}_2$  was prepared (Fig. 2c), different amount of  $\text{Co}_3\text{O}_4$  nanoparticles were dispersed into the raw materials, including 100 mg (Co to Mo is 6:13), 150 mg (Co to Mo is 9:13) and 200 mg (Co to Mo is 12:13), and the results were shown in Fig. 2d to Fig. 2f, respectively. The uniform dispersion of the  $\text{Co}_3\text{O}_4$  nanoparticles on  $\text{MoS}_2$  nanoflowers should contribute to the synthesis method using ZIFs as precursors, as effectively reduces the aggregation of particles. The energy dispersive X-ray spectroscopy (EDX) mapping of  $\text{Co}_3\text{O}_4$ @ $\text{MoS}_2$  composites (Fig. 2g) demonstrated the uniform distribution of Co, Mo, O, and S elements.

To further illustrate the crystal structure of  $Co_3O_4@MoS_2$ , the powder X-ray diffraction (XRD) spectra are measured for three different  $Co_3O_4@MoS_2$  composites (Fig. 3a). The distinct characteristic peaks at  $19.9^{\circ}$ ,  $31.3^{\circ}$ ,  $36.8^{\circ}$ ,  $59.3^{\circ}$ , and  $68.6^{\circ}$  can be assigned to (111), (220), (311), (511), and (440) crystallographic planes of  $Co_3O_4$  (PDF no. 42–1467), as demonstrates that the  $Co_3O_4$  particles are synthesized successfully. The additional peaks at  $32.3^{\circ}$ ,  $39.8^{\circ}$ ,  $46.2^{\circ}$ , and  $54.9^{\circ}$  in the XRD pattern of the composite are attributed to (100), (101), (102), and (110) crystal faces of CoMoS (PDF no.16–0105), as indicates the formation of Co-S bond. Therefore, the  $Co_3O_4$  nanoparticles is successfully

anchored on MoS<sub>2</sub> nanoflower support by Co-S coordination bond.

The chemical composition and oxidation state of the surface of Co<sub>3</sub>O<sub>4</sub>@MoS<sub>2</sub> are measured by X-ray photoelectron spectroscopy (XPS). In Fig. 3b, the peaks at 162.08, 232.08, 284.08, 395.08, 534.08, and 781.08 eV in the full spectra correspond to S 2p, Mo 3d, C 1 s, Mo 3p, O 1 s, and Co 2p, respectively, indicating the presence of Co, O, Mo, S. This is consistent with the elemental results measured by SEM elemental maps (Fig. 2g). As shown in Fig. 3c, the Co 2p spectrum can be fitted with two spin-orbit doublets for Co<sup>2+</sup> (785.13 and 802.69 eV) and Co<sup>3+</sup> (780.96 and 797.68 eV). The two peaks in the O 1 s spectra (Fig. 3d) at the binding energies of 531.24 and 532.70 eV correspond to metal-oxygen bonds and hydroxyl groups. Similarly, the Mo 3d spectrum (shown in Fig. 3e) can be fitted with two spin-orbit doublets for the Mo  $3d_{3/2}$ (232.02 eV) and Mo  $3d_{5/2}$  (228.54 eV) orbitals of the tetravalent molybdenum ion. The two peaks measured in the spectrum of S 2p are S  $2p_{3/2}$  and S  $2p_{1/2}$  orbitals at 161.33 and 162.62 eV (Fig. 3), respectively. In addition, the unlabeled peaks in the XPS spectrum are the satellite peaks. The above description proves the successful fabrication of Co<sub>3</sub>O<sub>4</sub>@MoS<sub>2</sub> without any impurities.

#### 3.2. ENO<sub>3</sub>RR performance of the electrocatalysts

To study the catalytic activity of Co<sub>3</sub>O<sub>4</sub>@MoS<sub>2</sub> for eNO<sub>3</sub>RR, the linear sweep voltammetry (LSV) measurements are carried out firstly in Na<sub>2</sub>SO<sub>4</sub> solution in the absence and presence of NO<sub>3</sub>, respectively (Fig. 4a). As the potential is more negative than -0.24 V, the current density of Co<sub>3</sub>O<sub>4</sub>@MoS<sub>2</sub> in the presence of NO<sub>3</sub> is significantly higher than that in the absence of NO<sub>3</sub>. It demonstrates that the eNO<sub>3</sub>RR occurs on  $Co_3O_4@MoS_2$  as the potential is lower than -0.24 V. The synthesized NH3 in the electrolyte are measured by UV-Vis spectrophotometry after maintaining a certain potential. Firstly, the voltage selected for testing is based on the results of LSV, the polarization curves are tested with Co<sub>3</sub>O<sub>4</sub>@MoS<sub>2</sub> as a catalyst and exhibit the eNO<sub>3</sub>RR activity in the negative potential lower than -0.24 V. Then the catalytic performance is tested with the voltage range of -0.94 V to -0.24 V (Fig. S3a). It can be seen that the Faradaic efficiency gradually decreased due to the accumulation of catalyst surface charge and the effect of hydrogen evolution reaction (HER) occupied more active sites at higher negative voltages [36]. The absorbance in UV-Vis spectra becomes higher with the increase of voltage (Figs. S3b and c), as means the yield of ammonia increases. The higher rate of NH<sub>3</sub> is due to the fact that a larger negative potential exerts a greater thermodynamic driving force for the reaction than a lower potential does. Considering the optimal voltage and FE changes, the voltage from - 0.64 V to - 0.24 V is selected to test the catalyst performance (Fig. S4). According to the measured NH3 concentrations, the yield and FE of Co<sub>3</sub>O<sub>4</sub>@MoS<sub>2</sub> with three different Co<sub>3</sub>O<sub>4</sub> loadings (100 mg, 150 mg, and 200 mg) are shown in Figs. 4b and 4c. The loading of Co<sub>3</sub>O<sub>4</sub> has a major effect on the activity of the Co<sub>3</sub>O<sub>4</sub>@MoS<sub>2</sub> catalyst and the catalytic performance is the highest when the loading of Co<sub>3</sub>O<sub>4</sub> is 150 mg. Moreover, the effect of electrical potential is explored. At the optimum potential, the NH3 yield rate reaches

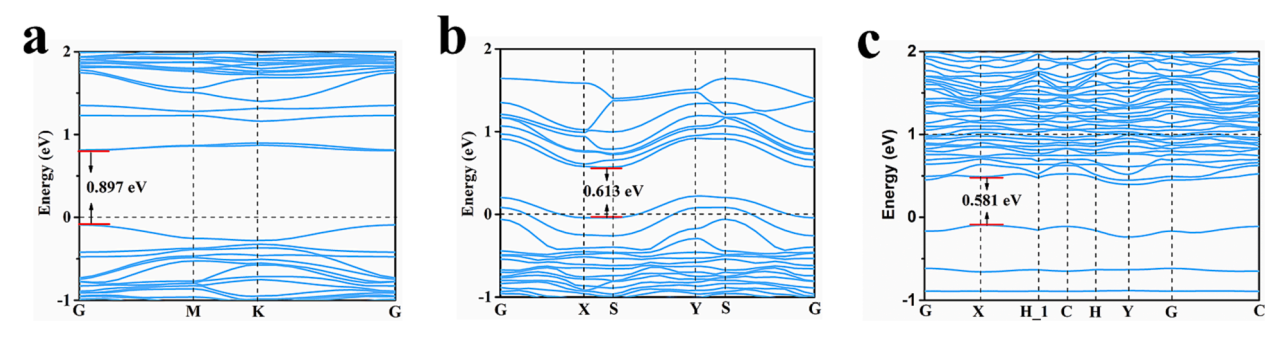


Fig. 5. Band diagram of (a) MoS<sub>2</sub>, (b) Co<sub>3</sub>O<sub>4</sub>, (c) Co<sub>3</sub>O<sub>4</sub>@MoS<sub>2</sub>.

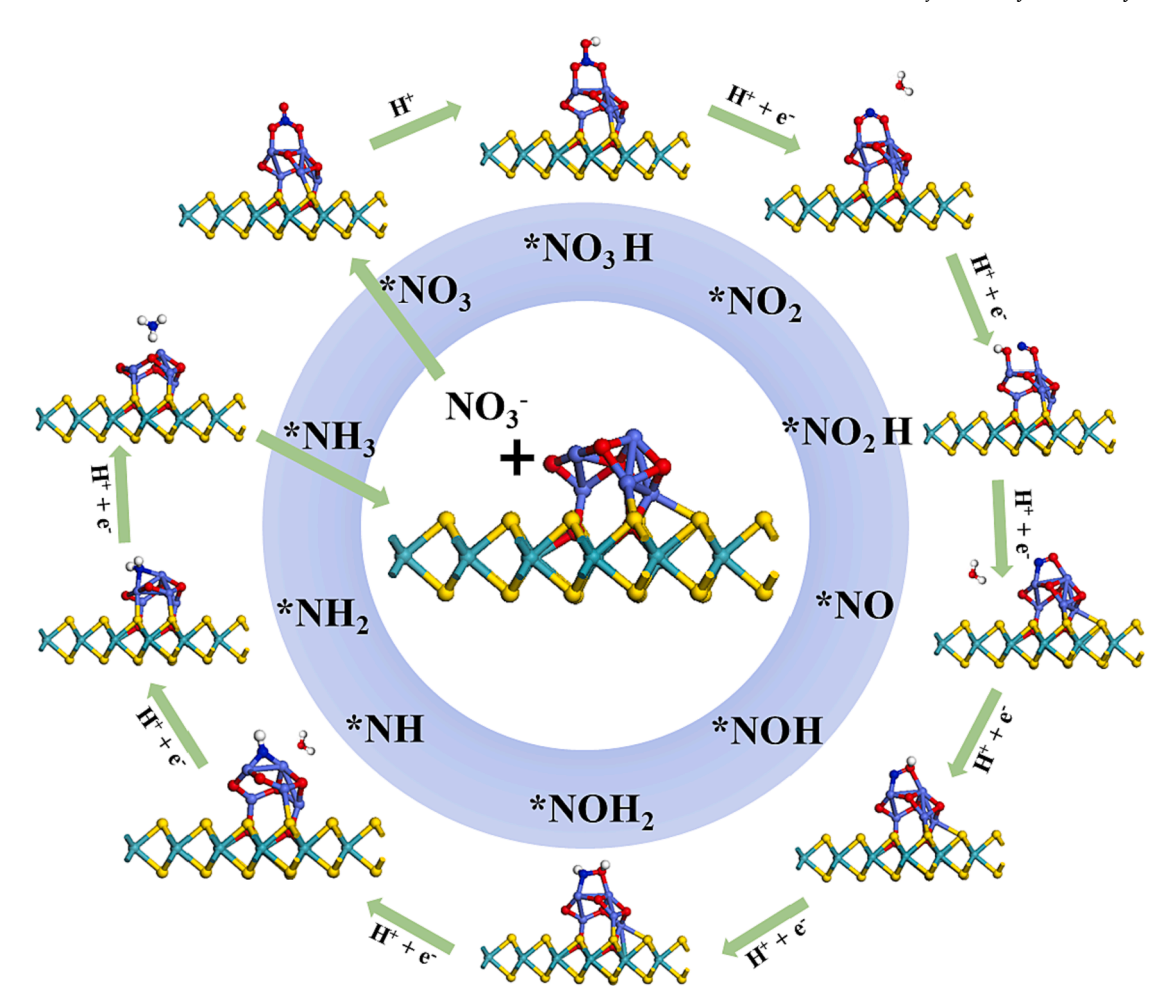


Fig. 6. Intermediates of all optimized structures of the Co<sub>3</sub>O<sub>4</sub>@MoS<sub>2</sub> eNO<sub>3</sub>RR reaction process (atomic colors represent: yellow, S; green, Mo; blue, N; red, O; purple, Co; white, H).

4539.61  $\mu g \ h^{-1} \ mg_{cat}^{-1}$  and the FE is 52.69% with the  $Co_3O_4$  loading of 150 mg at -0.64 V. As the potential increases, the FE of  $Co_3O_4@MoS_2$ increases continuously, and the maximum value is 85.05% at the optimum potential of -0.24 V. Compared to Co<sub>3</sub>O<sub>4</sub> and MoS<sub>2</sub>, Co<sub>3</sub>O<sub>4</sub>@MoS<sub>2</sub> exhibits excellent NH3 yield rate and FE under the same test conditions (as shown in Figs. 4d and 4e), implying that the combination of Co<sub>3</sub>O<sub>4</sub> and MoS<sub>2</sub> can accelerate the process of eNO<sub>3</sub>RR. And Co<sub>3</sub>O<sub>4</sub>@MoS<sub>2</sub> showed a combination of performance as good as most of the material previously reported (Table S1). Co<sub>3</sub>O<sub>4</sub>@MoS<sub>2</sub> shows such a superior performance because the combination of Co<sub>3</sub>O<sub>4</sub> and MoS<sub>2</sub> reduces the bandwidth, improves electronic conductivity and surface chemical active sites, which will be discussed in the theoretical calculations. The FE and NH<sub>3</sub> yield rate at the optimum potentials of Co<sub>3</sub>O<sub>4</sub> and MoS<sub>2</sub> are 50.67% and 16% at - 0.24 V, 2048.63  $\mu g~h^{-1}~mg_{cat}^{-1}$  and 675.01  $\mu g~h^{-1}$  $mg_{cat}^{-1}$  at -0.64 V, respectively. The above observations indicate that the performance exhibited by Co<sub>3</sub>O<sub>4</sub>@MoS<sub>2</sub> varies with the amount of Co<sub>3</sub>O<sub>4</sub> on the composite. So, it can be speculated that the active site of eNO<sub>3</sub>RR in the Co<sub>3</sub>O<sub>4</sub>@MoS<sub>2</sub> composite should populate on the Co atom.

In order to investigate the selectivity of the  $\text{Co}_3\text{O}_4\text{@MoS}_2$  catalyst, the main byproduct of  $\text{NO}_2^-$  has been detected and calculated by UV–Vis (Fig. S5). As shown in Fig. 4f, the FE of  $\text{NO}_2^-$  starts from an onset potential of 5% and then gradually decreases to about 2%. This trend is the same as the conversion of  $\text{NO}_3^-$  to  $\text{NH}_3$ , suggesting that the synthesis of  $\text{NH}_3$  is followed by the formation of  $\text{NO}_2^-$  at each applied potential. And the yield rate of  $\text{NO}_2^-$  increases distinctly after - 0.44 V (Fig. S5c), but the overall concentration of  $\text{NO}_2^-$  was still at a low level. In addition, the presence of  $\text{N}_2\text{H}_4$  was hardly observed in the electrolyte after electrolysis at the applied voltage (Fig. S6). In general, the byproducts are negligible

compared to the FE and yield rate of  $NH_3$ , which indicates that  $\text{Co}_3\text{O}_4@\text{MoS}_2$  has excellent selectivity for the conversion from  $NO_3^-$  to  $NH_2$ .

Subsequently, it is proceeded to electrolysis for a total of 7 cycles in 0.1 M  $Na_2SO_4$  (with and without  $NO_3^-$ ) at -0.64 V (Fig. 4g) to confirm the origin of  $NH_3$ . The  $NH_3$  was obtained only in the electrolyte with  $NO_3^-$  and the performance remained stable after the alternating test. Furthermore, the  $^{15}N$  isotopic labeling experiments also confirmed the origin of  $NH_3$ . As shown in Fig. 4h, the proton nuclear magnetic resonance ( $^1H$  NMR) spectra show only double characteristic peaks of  $^{15}NH_4^+$  and triple characteristic peaks of  $^{14}NH_4^+$  when  $^{15}NO_3^-$  and  $^{14}NO_3^-$  are used as raw materials. The above results indicated that  $NO_3^-$  is the only nitrogen source for  $NH_3$  synthesis rather than others.

The stability of the catalyst is another vital factor to evaluate the practical application in  $eNO_3RR$ . As shown in Fig. S7a, the current density at - 0.64 V has been measured for 24 h. The curve has no obvious fluctuations and the overall trend is relatively stable. In general, the current density exhibits good stability over 24 h, indicating the stable conductivity and durability of the catalyst. Furthermore, the NH<sub>3</sub> yield rate and FE at - 0.64 V were test for 10 cycles as shown in Fig. 4i. It can be seen that the NH<sub>3</sub> yield rate and FE fluctuate slightly and remain above 4588  $\mu g \ h^{-1} \ mg_{cal}^{-1}$  and 52%, respectively. As shown in Figs. S7b and S7c, the current density and absorbance almost keep constant during the 10-cycle test. Importantly, SEM images (Fig. S7d) reveal that  $Co_3O_4@MoS_2$  with  $Co_3O_4$  loadings of 150 mg still maintains its nanoflower and the presence of the loadings was also clearly visible after the eNO<sub>3</sub>RR experiment. Therefore, the conclusion can be drawn that the catalyst has excellent activity and stability with bright future in

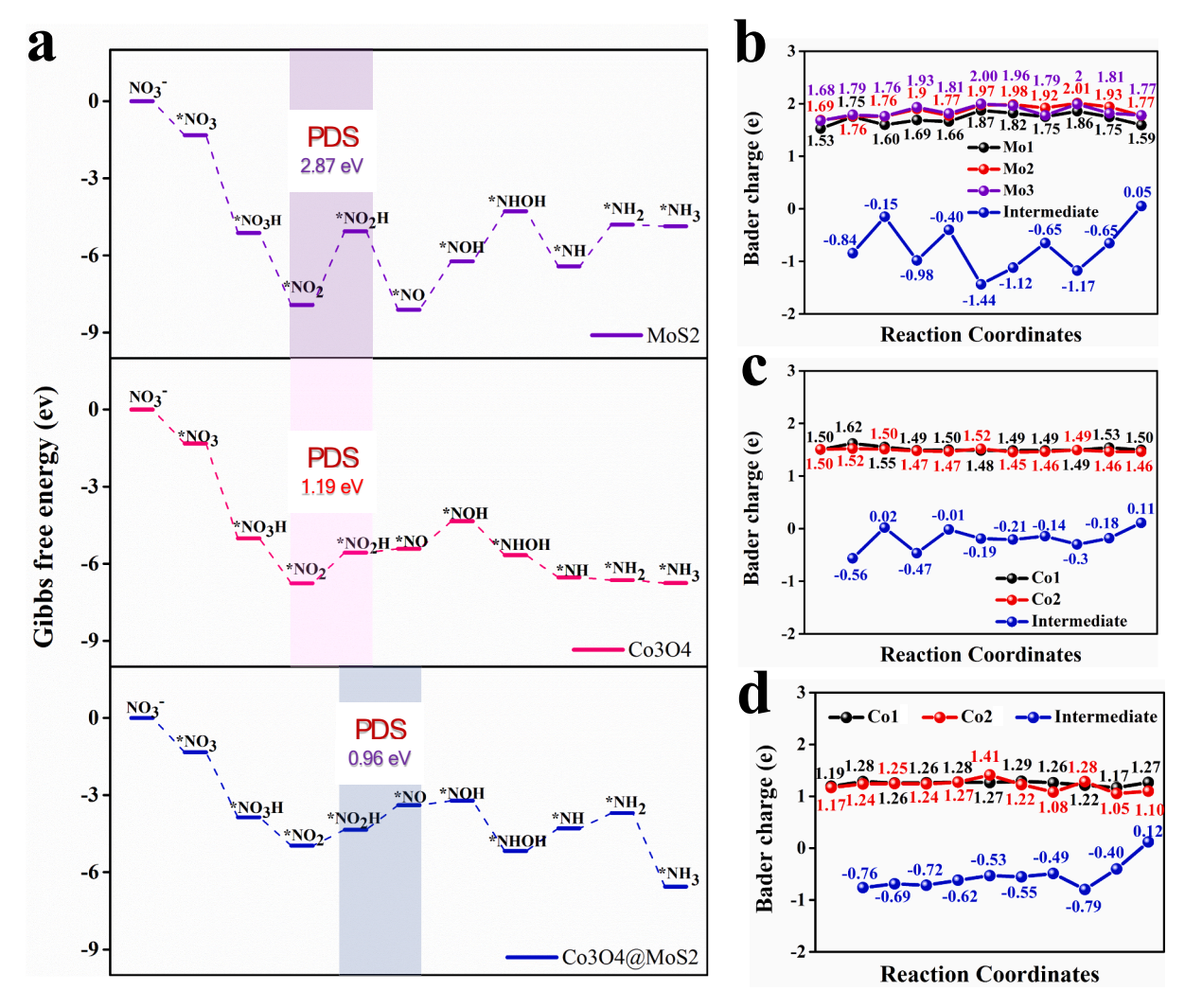


Fig. 7. (a) Free energy changes in each step of the reaction processes of  $MoS_2$ ,  $Co_3O_4$ , and  $Co_3O_4@MoS_2$ . The calculated Bader charges of the active site and intermediate on (b)  $MoS_2$ , (c)  $Co_3O_4$ , and (d) $Co_3O_4@MoS_2$ .

commercial application.

## 3.3. Mechanisms study for eNO<sub>3</sub>RR

To reveal the essence of excellent performance in nitrate reduction, the reaction mechanism has been studied employing the DFT calculations. The structures of  $\text{Co}_3\text{O}_4$ ,  $\text{MoS}_2$ , and  $\text{Co}_3\text{O}_4$ @ $\text{MoS}_2$  are designed based on the characterization results using metal atoms as active sites (Fig. S8). It is found that new Co-S bonds are formed between  $\text{Co}_3\text{O}_4$  and  $\text{MoS}_2$  during the  $\text{Co}_3\text{O}_4$ @ $\text{MoS}_2$  structural optimization, which is consistent with the XRD results. The energy bands of three catalysts are calculated and presented in Fig. 5. It can be clearly seen that the energy band of  $\text{MoS}_2$ ,  $\text{Co}_3\text{O}_4$ , and  $\text{Co}_3\text{O}_4$ @ $\text{MoS}_2$  is 0.897, 0.613, and 0.581 eV, respectively. Therefore,  $\text{Co}_3\text{O}_4$ @ $\text{MoS}_2$  has better electronic conductivity than its individual materials, which also provides better electron transfer for eNO<sub>3</sub>RR process.

The reduction of nitrate to ammonia is accompanied by the transfer of eight proton-coupled-electrons and the overall pathway of the reaction can be described by the following equation:

$$NO_3^- + 9H^+ + 8e^- \rightarrow NH_3 + 3H_2O$$

Fig. 6 and Fig. S9 show the minimum energy pathway for the reduction of nitrate to  $NH_3$  at the active site. The first step of the reaction is the adsorption of nitrate. To avoid the influence of negatively charged  $NO_3$  on the calculated results, a thermodynamic cycle from  $NO_3$  to  $NO_3$ 

 $(NO_3^-(l) \to HNO_3(l) \to HNO_3(g) \to NO_3(g))$  has been adapted (Fig. S10) [34]. Taking into account the changes in entropy and enthalpy during liquid to gaseous conversion from  $NO_3^-$  to  $NO_3$ , an energy of 0.75 eV has been used to correct the free energy of  $NO_3^-$  [34,35]. The formula for calculating the Gibbs free energy in solution before nitrate adsorption is as follows:

$$\Delta G_{NO_3} = E(*NO_3) + \frac{1}{2}E(H_2) - E(*) - E(HNO_3) + 0.75eV$$

where  $E(*NO_3)$  is the energy of NO<sub>3</sub> adsorbed on the catalyst system,  $E(H_2)$  refers to the energy of gaseous H<sub>2</sub> molecule, E(\*) denotes the energy of the catalyst alone, and  $E(HNO_3)$  is the energy of HNO<sub>3</sub> molecule. Then, the Gibbs free energies of each elementary step for the complete processes of MoS<sub>2</sub>, Co<sub>3</sub>O<sub>4</sub>, and Co<sub>3</sub>O<sub>4</sub>@MoS<sub>2</sub> are calculated by the pathway: \*NO<sub>3</sub>  $\rightarrow$  \*NO<sub>3</sub>H  $\rightarrow$  \*NO<sub>2</sub>  $\rightarrow$  \*NO<sub>2</sub>H  $\rightarrow$  \*NO  $\rightarrow$  \*NOH  $\rightarrow$  \*NHOH  $\rightarrow$  \*NH  $\rightarrow$  \*NH<sub>2</sub>  $\rightarrow$  \*NH<sub>3</sub>(g) [34].

The variations of the Gibbs free energy and the charge in each elementary step along the reaction pathway of  $NO_3^-$  electroreduction to ammonia on  $MoS_2$ ,  $Co_3O_4$ , and  $Co_3O_4$ @ $MoS_2$  catalysts are collected in Fig. 7. It can be observed clearly that the elementary steps of  $NO_3^-$  adsorption, the proton-electron pair combination, and the first dehydration are all exothermic processes. This is in accordance with the results reported recently [37,38]. The subsequent hydrogenation of \* $NO_2^-$  to produce \* $NO_2^-$ H is endothermic distinctly. The Gibbs free energy is enhanced by 2.87 eV when the conversion from \* $NO_2^-$  to \* $NO_2^-$ H occurs

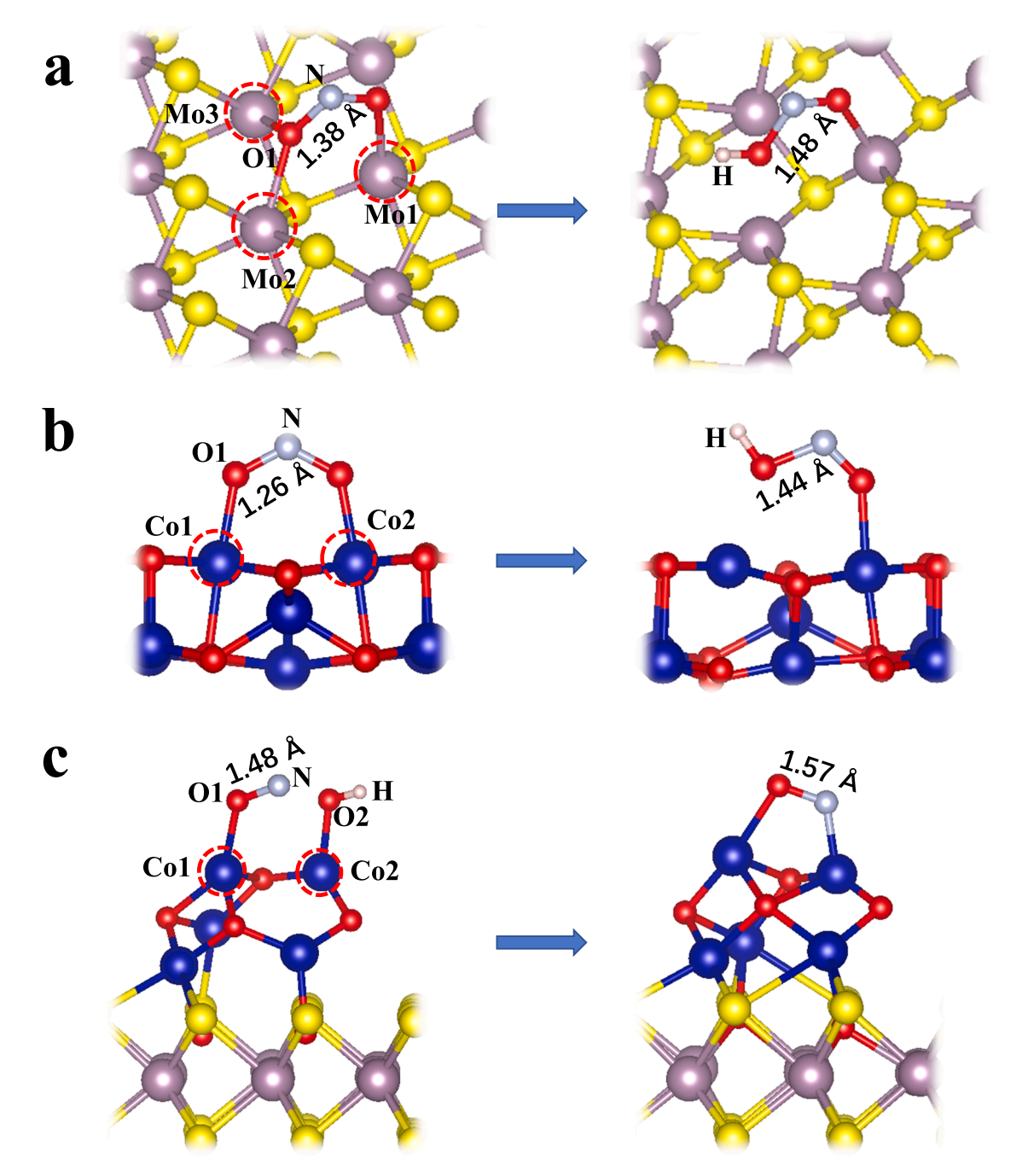


Fig. 8. The structural model changes at PDS for (a) Co<sub>3</sub>O<sub>4</sub>, (b) MoS<sub>2</sub> and (c) Co<sub>3</sub>O<sub>4</sub>@MoS<sub>2</sub> (atomic colors represent: yellow, S; purple, Mo; gray, N; red, O; blue, Co; white, H).

on MoS $_2$  surface, accompanied by significant electron transfer (0.58 e) between the intermediate and the catalyst. It is taken as the potential determining step (PDS). As the catalyst varies from MoS $_2$  to Co $_3$ O $_4$ , the Gibbs free energy is raised by 1.19 eV and the transferred electron is 0.46 e. It also corresponds to the PDS. While for the Co $_3$ O $_4$ @MoS $_2$  composite, the variation of Gibbs free energy for this hydrogenation is 0.62 eV and transferred electron is 0.1 e. While the Gibbs free energy of the subsequent formation of \*NO (\*NO $_2$ H  $\rightarrow$  \*NO) increases distinctly by 0.96 eV, which is taken as the PDS.

The geometrical structures of the PDS from \*NO $_2$  to \*NO $_2$ H are optimised (Fig. 8). The generation of O1-H bond on MoS $_2$  is followed by the broken of both Mo2-O1 and Mo3-O1 bonds, the elongation of N-O1 bond from 1.38 Å to 1.48 Å (Fig. 8a), as well as the charge variation from - 0.87  $\it e$  on O1 to - 0.20  $\it e$  on O1H group. The strong interaction

between Mo and O1 leads to the immersion of O1 (in the plane of sulfurs) and the bulging of N, as is disadvantageous structurally to the subsequent combination of proton-electron pair. Similarly, the formation of O1-H bond on  $\text{Co}_3\text{O}_4$  is accompanied by the Co1-O1 bond broken, the N-O1 bond extension from 1.26 Å to 1.44 Å (Fig. 8b), and the increase of charges from - 0.51 e on O1 to - 0.09 e on O1H group. It indicates the weakening of both Co1-O1 and N-O1 interactions. In addition, the O1 stands on the surface of  $\text{Co}_3\text{O}_4$ , as favors the following combination of next proton-electron pair and the consequent dehydration reaction. In the \*NO<sub>2</sub>H  $\rightarrow$  \*NO process on  $\text{Co}_3\text{O}_4$ @MoS<sub>2</sub>, more obvious structural changes are observed: the broken of Co2-O2 bond, the departure of dissociated OH group, the formation of Co2-N bond, and the extension of N-O bond from 1.48 Å to 1.57 Å and the Co1-O1 bond extension from 1.97 Å to 2.11 Å (Fig. 8c). The O replaces N as the most

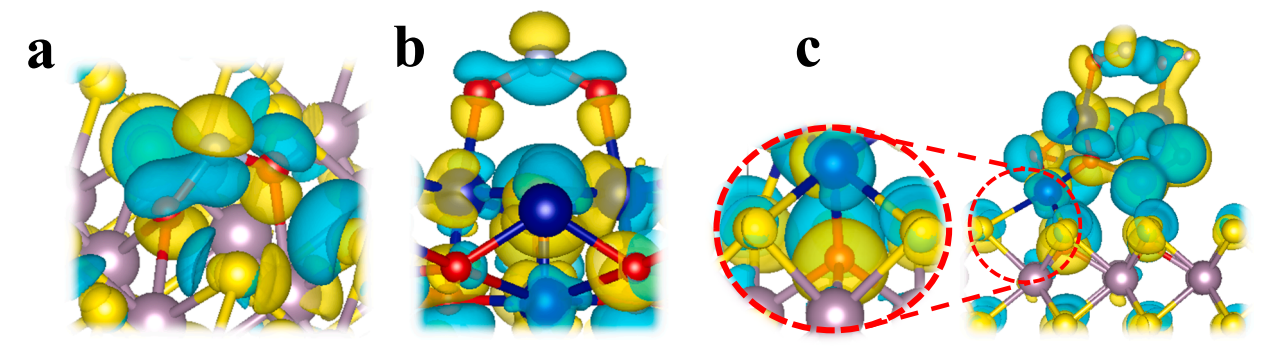


Fig. 9. The charge density difference of (a) MoS<sub>2</sub>, (b) Co<sub>3</sub>O<sub>4</sub>, and (c) Co<sub>3</sub>O<sub>4</sub>@MoS<sub>2</sub> (atomic colors represent: yellow, S; purple, Mo; gray, N; red, O; blue, Co; white, H. Electron density cloud color: yellow, charge accumulation: blue, charge depletion).

exposed atom, facilitating the next step of hydrogenation. During the \*NO<sub>2</sub>H  $\rightarrow$  \*NO process on Co<sub>3</sub>O<sub>4</sub>@MoS<sub>2</sub>, MoS<sub>2</sub> transfers 0.35 e to Co<sub>3</sub>O<sub>4</sub> and the intermediate. There are more charge accumulation compared to those on the independent Co<sub>3</sub>O<sub>4</sub>. In addition, in the O1-N group on Co<sub>3</sub>O<sub>4</sub>@MoS<sub>2</sub>, the charge on O1 decreases by 0.04 e while the N charge increases by 0.34 e, indicating that the Co2-N interaction increases while the Co1-O1-N coupling decreases, which facilitates the next step of deoxygenation. In contrast, the charge on O1 and N in the O1-N group on the independent Co<sub>3</sub>O<sub>4</sub> increases by 0.27 e and 0.01 e respectively, and the enhanced interaction between Co2-O1 is not conducive to the next step of deoxygenation. Therefore, MoS<sub>2</sub> in Co<sub>3</sub>O<sub>4</sub>@MoS<sub>2</sub> does not directly participate in the reaction as an active site but also plays a nonnegligible role.

The charge density differences of the PDS step on three catalysts are represented in Fig. 9. With MoS<sub>2</sub> as a catalyst, the charge depletion between O1-N and the accumulation between Mo-O1 observed in Fig. 9a indicate that more electrons populate on O1, as is in accordance with the former discussion about the charges. Fig. 9b shows distinct charge depletion between O-N and charge accumulation between Co-O, which implies that the Co<sub>3</sub>O<sub>4</sub> cluster can serve as a nitrate-activated center. In the case of Co<sub>3</sub>O<sub>4</sub>@MoS<sub>2</sub> (Fig. 9c), the oxygen atom accumulates a large charge, which makes deoxygenation easier, as the energy accumulation after the oxygen hydrogenation step leads to the breaking of the N-O bond. Furthermore, the electron depletion and accumulation of Co<sub>3</sub>O<sub>4</sub>@MoS<sub>2</sub> locate mainly on Co<sub>3</sub>O<sub>4</sub>, as indicates that the immediate active site of the reaction is on Co<sub>3</sub>O<sub>4</sub>. The charge distribution on the surface of Co and S atoms also reflects the new Co-S bond as a bridge for charge transfer between MoS<sub>2</sub> and Co<sub>3</sub>O<sub>4</sub>, which corresponds to the previous charge transfer situation, further demonstrating the synergistic role played by MoS2 in the catalyst. It attributes to the lower energy barrier of Co<sub>3</sub>O<sub>4</sub>@MoS<sub>2</sub> as compared tothose of Co<sub>3</sub>O<sub>4</sub> and MoS<sub>2</sub>. The theoretical results show that the catalytic performance of Co<sub>3</sub>O<sub>4</sub>@MoS<sub>2</sub> is significantly improved, which is in consistent with the experimental results.

#### 4. Conclusion

The use of ZIF-67 as a precursor to synthesize  $\text{Co}_3\text{O}_4$  effectively reduces the volume of nanoparticles, then the use of  $\text{MoS}_2$  as a support solves the problem of nanoparticle aggregation and provides a synergistic effect for the formation and coordination of S-Co to enhance the activity of the catalyst. Experiments show that  $\text{Co}_3\text{O}_4\text{@MoS}_2$  has good catalytic activity, selectivity, and stability. It shows excellent FE and NH<sub>3</sub> yield rate of 52.69% and 4539.61 µg h<sup>-1</sup> mg\_{cal}^{-1} at -0.64 V, as is significantly improved as compare with those of  $\text{Co}_3\text{O}_4$ . DFT calculations show that  $\text{Co}_3\text{O}_4\text{@MoS}_2$  has lower energy barrier and smaller bandwidth than those of  $\text{Co}_3\text{O}_4$  and  $\text{MoS}_2$ , proving that the  $\text{Co}_3\text{O}_4\text{@MoS}_2$  has better performance for eNO<sub>3</sub>RR than  $\text{Co}_3\text{O}_4$  and  $\text{MoS}_2$ . This study proposes an effective solution to the problem of metal oxide

nanoparticle aggregation, and future research needs to carry out for nitrate reduction tests in the protection of resources and environment.

#### CRediT authorship contribution statement

Yanli Zhang: Writing – original draft, Investigation. Jiuqing Xiong: Validation, Data curation. Shihai Yan: Supervision, Funding acquisition, Writing – review & editing. Bingping Liu: Conceptualization, Methodology, Writing – review & editing.

#### **Declaration of Competing Interest**

The authors declare that they have no known competing financial interests or personal relationships that could have appeared to influence the work reported in this paper.

# Acknowledgements

This work was supported by the National Natural Science Foundation of China (Grant No. 21203227), Natural Science Foundation of Shandong Province (Grant No. ZR2016BM33), the Research Foundation for Talented Scholars of Qingdao Agricultural University (No. 6631120039 & 6631113335), National College Student Innovation and Entrepreneurship Training Program (S202010435041), and the open fund of the state key laboratory of molecular reaction dynamics in DICP, CAS. The authors would like to thank Zhao Baobao from Shiyanjia Lab (www.shiyanjia.com) for the XPS analysis.

## Appendix A. Supplementary data

Supplementary data to this article can be found online at https://doi.org/10.1016/j.jelechem.2023.117702.

#### References

- N.a. Cao, G. Zheng, Aqueous electrocatalytic N<sub>2</sub> reduction under ambient conditions. Nano Res. 11 (6) (2018) 2992–3008.
- [2] Y. Huang, D.D. Babu, Z. Peng, Y. Wang, Atomic Modulation, Structural Design, and Systematic Optimization for Efficient Electrochemical Nitrogen Reduction, Adv. Sci. 7 (4) (2020) 1902390.
- [3] Q. Liu, L. Xie, J. Liang, Y. Ren, Y. Wang, L. Zhang, L. Yue, T. Li, Y. Luo, N.a. Li, B. o. Tang, Y. Liu, S. Gao, A.A. Alshehri, I. Shakir, P.O. Agboola, Q. Kong, Q. Wang, D. Ma, X. Sun, Ambient Ammonia Synthesis via Electrochemical Reduction of Nitrate Enabled by NiCo<sub>2</sub>O<sub>4</sub> Nanowire Array, Small 18 (13) (2022) e2106961.
- [4] J.i. Li, Y. Zhang, C. Liu, L. Zheng, E. Petit, K. Qi, Y. Zhang, H. Wu, W. Wang, A. Tiberj, X. Wang, M. Chhowalla, L. Lajaunie, R. Yu, D. Voiry, 3.4% Solar-to-Ammonia Efficiency from Nitrate Using Fe Single Atomic Catalyst Supported on MoSo Nanosheets. Adv. Funct. Mater. 32 (18) (2022) 2108316.
- [5] V. Smil, Detonator of the population explosion, Nature 400 (6743) (1999) 415.
- [6] T. Wu, X. Zhu, Z. Xing, S. Mou, C. Li, Y. Qiao, Q. Liu, Y. Luo, X. Shi, Y. Zhang, X. Sun, Greatly Improving Electrochemical N<sub>2</sub> Reduction over TiO<sub>2</sub> Nanoparticles by Iron Doping, Angew. Chem. Int. Ed. 58 (51) (2019) 18449–18453.

- [7] G. Soloveichik, Electrochemical synthesis of ammonia as a potential alternative to the Haber-Bosch process, Nat. Catal. 2 (2019) 377–380.
- [8] B. Suryanto, H.L. Du, D. Wang, J. Chen, A.N. Simonov, D.R. Macfarlane, Challenges and prospects in the catalysis of electroreduction of nitrogen to ammonia, Nat. Catal. 2 (2019) 290–296.
- [9] C. Guo, J. Ran, A. Vasileff, S.-Z. Qiao, Rational design of electrocatalysts and photo (electro) catalysts for nitrogen reduction to ammonia (NH<sub>3</sub>) under ambient conditions, Energ. Environ. Sci. 11 (1) (2018) 45–56.
- [10] Y. Wan, J. Xu, R. Lv, Heterogeneous electrocatalysts design for nitrogen reduction reaction under ambient conditions, Mater. Today 27 (2019) 69–90.
- [11] J. Wen, H. Chang, T. Huang, M. Hossain, Z. Liu, H. Sun, Y. Zhu, Y. Chen, Q. Huang, Y. Wu, A simple synthesis of Co<sub>3</sub>O<sub>4</sub>@CNT to boost electrochemical nitrogen fixation, Electrochim. Acta 367 (2021).
- [12] T. Mou, J. Long, T. Frauenheim, J. Xiao, Advances in Electrochemical Ammonia Synthesis Beyond the Use of Nitrogen Gas as a Source, ChemPlusChem 86 (8) (2021) 1211–1224.
- [13] Z. Ning, J. Abdul, D. Chen, S. Liu, Y. Gao, Refining Defect States in W<sub>18</sub>O<sub>49</sub> by Mo Doping: A Strategy for Tuning N-2 Activation towards Solar-Driven Nitrogen Fixation, J. Am. Chem. Soc. 140 (2018) 9434–9443.
- [14] M.A. Kaczmarek A. Malhotra B. GA, A. Timmins, S.P. Devisser, Nitrogen Reduction to Ammonia on a Biomimetic Mononuclear Iron Centre: Insights into the Nitrogenase Enzyme Wiley-Blackwell Online Open 24 2018 1 11.
- [15] Y. Luo, G.-F. Chen, L.i. Ding, X. Chen, L.-X. Ding, H. Wang, Efficient Electrocatalytic N<sub>2</sub> Fixation with MXene under Ambient Conditions, Joule 3 (1) (2019) 279–289.
- [16] L. Zeng, X. Li, S. Chen, J. Wen, F. Rahmati, J. van der Zalm, A. Chen, Highly boosted gas diffusion for enhanced electrocatalytic reduction of N<sub>2</sub> to NH<sub>3</sub> on 3D hollow Co–MoS<sub>2</sub> nanostructures, Nanoscale 12 (10) (2020) 6029–6036.
- [17] J. Li, D. Zhao, L. Zhang, L. Yue, Y. Luo, Q. Liu, N.a. Li, A.A. Alshehri, M.S. Hamdy, Q. Li, X. Sun, A FeCo<sub>2</sub>O<sub>4</sub> nanowire array enabled electrochemical nitrate conversion to ammonia, Chem. Commun. (Camb) 58 (28) (2022) 4480–4483.
- [18] Z. Li, G. Wen, J. Liang, T. Li, Y. Luo, Q. Kong, X. Shi, A.M. Asiri, Q. Liu, X. Sun, High-efficiency nitrate electroreduction to ammonia on electrodeposited cobalt–phosphorus alloy film, Chem. Commun. 57 (76) (2021) 9720–9723.
- [19] P. Song, G. Huang, Y. Hong, C. An, X. Xin, P. Zhang, A biophysiological perspective on enhanced nitrate removal from decentralized domestic sewage using gravitational-flow multi-soil-layering systems, Chemosphere 240 (2020), 124868.
- [20] J.O. Lundberg, E. Weitzberg, J.A. Cole, N. Benjamin, Nitrate, bacteria and human health, Nat. Rev. Microbiol. 2 (7) (2004) 593–602.
- [21] P. Huang, T. Fan, X. Ma, J. Zhang, Y. Zhang, Z. Chen, X. Yi, 3D flower-like zinc cobaltite for electrocatalytic reduction of nitrate to ammonia under ambient conditions. ChemSusChem 15 (2022) e202102049.
- [22] J. Gao, B.o. Jiang, C. Ni, Y. Qi, X. Bi, Enhanced reduction of nitrate by noble metal-free electrocatalysis on P doped three-dimensional Co<sub>3</sub>O<sub>4</sub> cathode: mechanism exploration from both experimental and DFT studies, Chem. Eng. J. 382 (2020), 123034.
- [23] C. Li, K. Li, C. Chen, Q. Tang, T. Sun, J. Jia, Electrochemical removal of nitrate using a nanosheet structured Co<sub>3</sub>O<sub>4</sub>/Ti cathode: effects of temperature, current and pH adjusting, Sep. Purif. Technol. 237 (2020), 116485.
- [24] Y. Gong, J. Wu, M. Kitano, J. Wang, T.-N. Ye, J. Li, Y. Kobayashi, K. Kishida, H. Abe, Y. Niwa, H. Yang, T. Tada, H. Hosono, Ternary intermetallic LaCoSi as a catalyst for N<sub>2</sub> activation, Nat. Catal. 1 (3) (2018) 178–185.
- [25] L. Zhou, S. Cao, L. Zhang, G. Xiang, J. Wang, X. Zeng, J. Chen, Facet effect of Co<sub>3</sub>O<sub>4</sub> nanocatalysts on the catalytic decomposition of ammonium perchlorate, J. Hazard. Mater. 392 (2020). 122358.
- [26] L.-Y. Zhou, S.-B. Cao, L.-L. Zhang, G. Xiang, X.-F. Zeng, J.-F. Chen, Promotion of the Co<sub>3</sub>O<sub>4</sub>/TiO<sub>2</sub> Interface on Catalytic Decomposition of Ammonium Perchlorate, ACS Appl. Mater. Interfaces 14 (2) (2022) 3476–3484.

- [27] B.H.R. Suryanto, D. Wang, L.M. Azofra, M. Harb, L. Cavallo, R. Jalili, D.R. G. Mitchell, M. Chatti, D.R. MacFarlane, MoS<sub>2</sub> polymorphic engineering enhances selectivity in the electrochemical reduction of nitrogen to ammonia, ACS Energy Lett. 4 (2) (2019) 430–435.
- [28] M.I. Ahmed, L.J. Arachchige, Z. Su, D.B. Hibbert, C. Sun, C. Zhao, Nitrogenase-Inspired Atomically Dispersed Fe-S-C Linkages for Improved Electrochemical Reduction of Dinitrogen to Ammonia, ACS Catal. 12 (2) (2022) 1443–1451.
- [29] G. Kresse, J. Furthmüller, Efficiency of ab-initio total energy calculations for metals and semiconductors using a plane-wave basis set - ScienceDirect, Comput. Mater. Sci 6 (1) (1996) 15–50.
- [30] M.D. Segall, P.J.D. Lindan, M.J. Probert, C.J. Pickard, P.J. Hasnip, S.J. Clark, M. C. Payne, First-principles simulation: ideas, illustrations and the CASTEP code, J. Phys.: Condens. 14 (Matter 2002,) 2717–2744.
- [31] P.E. Blöchl, Projector Augmented-Wave Method, Phys. Rev. B 50 (24) (1994) 17953–17979.
- [32] J.P. Perdew, K. Burke, M. Ernzerhof, Generalized Gradient Approximation Made Simple [Phys. Rev. Lett. 77, 3865 (1996)], Phys. Rev. Lett. 78 (7) (1997).
- [33] S. Grimme, Semiempirical GGA-type density functional constructed with a long-range dispersion correction, J. Comput. Chem. 27 (15) (2006) 1787–1799.
- [34] T. Hu, C. Wang, M. Wang, C.M. Li, C. Guo, Theoretical Insights into Superior Nitrate Reduction to Ammonia Performance of Copper Catalysts, ACS Catal. 11 (23) (2021) 14417–14427.
- [35] J.-X. Liu, D. Richards, N. Singh, B.R. Goldsmith, Activity and Selectivity Trends in Electrocatalytic Nitrate Reduction on Transition Metals, ACS Catal. 9 (8) (2019) 7052–7064
- [36] W. Nie, X. Wang, Z. Wang, Y. Gao, R. Chen, Y. Liu, C. Li, F. Fan, Identifying the Role of the Local Charge Density on the Hydrogen Evolution Reaction of the Photoelectrode, J. Phys. Chem. Lett. 12 (44) (2021) 10829–10836.
- [37] W.-J. Sun, L.-X. Li, H.-Y. Zhang, J.-H. He, J.-M. Lu, A Bioinspired Iron-Centered Electrocatalyst for Selective Catalytic Reduction of Nitrate to Ammonia, ACS Sustain. Chem. Eng. 10 (18) (2022) 5958–5965.
- [38] S. Wang, H. Gao, L. Li, K.S. Hui, D.A. Dinh, S. Wu, S. Kumar, F. Chen, Z. Shao, K. N. Hui, High-throughput identification of highly active and selective single-atom catalysts for electrochemical ammonia synthesis through nitrate reduction, Nano Energy 100 (2022), 107517.
- [39] Z. Deng, C. Ma, Z. Li, Y. Luo, L. Zhang, S. Sun, Q. Liu, J. Du, Q. Lu, B. Zheng, X. Sun, High-Efficiency Electrochemical Nitrate Reduction to Ammonia on a Co<sub>3</sub>O<sub>4</sub> Nanoarray Catalyst with Cobalt Vacancies, ACS Appl. Mater. Interfaces 14 (2022) 46595–46602.
- [40] X. Fan, C. Ma, D. Zhao, Z. Deng, L. Zhang, Y. Wang, Y. Luo, D. Zheng, T. Li, J. Zhang, S. Sun, Q. Lu, X. Sun, Unveiling selective nitrate reduction to ammonia with Co<sub>3</sub>O<sub>4</sub> nanosheets/TiO<sub>2</sub> nanobelt heterostructure catalyst, J. Colloid Interface Sci. 630 (2023) 714–720.
- [41] D.i. Liu, L. Qiao, Y. Chen, P. Zhou, J. Feng, C.C. Leong, K.W. Ng, S. Peng, S. Wang, W.F. Ip, H. Pan, Electrocatalytic reduction of nitrate to ammonia on low-cost manganese-incorporated Co3O4 nanotubes, Appl Catal B 324 (2023), 122293.
- [42] B. Fang, J. Yao, X. Zhang, L. Ma, Y. Ye, J. Tang, G. Zou, J. Zhang, L. Jiang, Y. Sun, A large scaled-up monocrystalline 3R MoS2 electrocatalyst for efficient nitrogen reduction reactions, New J. Chem. 45 (5) (2021) 2488–2495.
- [43] S. Luo, X. Li, B. Zhang, Z. Luo, M. Luo, MOF-Derived Co3O4@NC with Core-Shell Structures for N2 Electrochemical Reduction under Ambient Conditions, ACS Appl. Mater. Interfaces 11 (2019) 26891–26897.
- [44] C. Ma, D.a. Liu, Y. Zhang, J. Yong Lee, J. Tian, B. Liu, S. Yan, MOF-derived Fe2O3@MoS2: An efficient electrocatalyst for ammonia synthesis under mild conditions, Chem. Eng. J. 430 (2022), 132694.
- [45] C. Ma, N. Zhai, B. Liu, S. Yan, Defected MoS2: An efficient electrochemical nitrogen reduction catalyst under mild conditions, Electrochim. Acta 370 (2021), 137695.